Targeted Deposition of Platinum onto Gold Nanorods by Plasmonic Hot Electrons

Gregory T. Forcherio,* David R. Baker,* Jonathan Boltersdorf, Asher C. Leff, Joshua P. McClure, Kyle N. Grew, Cynthia A. Lundgren

Sensors & Electron Devices Directorate, U.S. Army Research Laboratory, Adelphi, MD 20783 USA

*E-mail: gregory.t.forcherio.ctr@mail.mil (G.T.F.)
*E-mail: david.r.baker175.civ@mail.mil (D.R.B.)

SUPPORTING INFORMATION

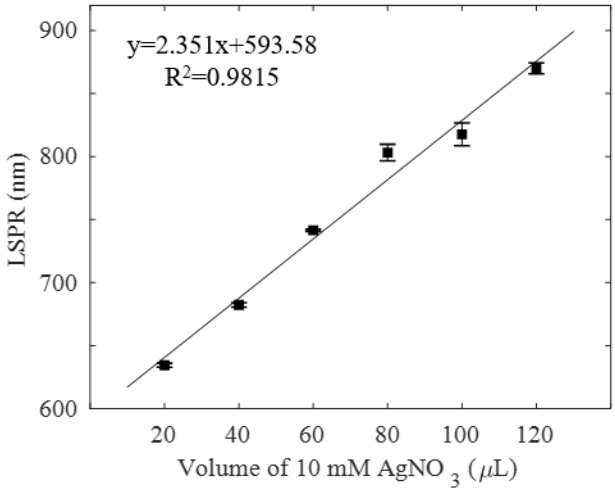

Figure S1. Calibration curve of AuNR LSPR wavelength in water versus volume of 10 mM $AgNO_3$ in the growth solution. Fitted linear relationship and R^2 value are inset. Data points are the mean from triplicate replication and error is one standard deviation.

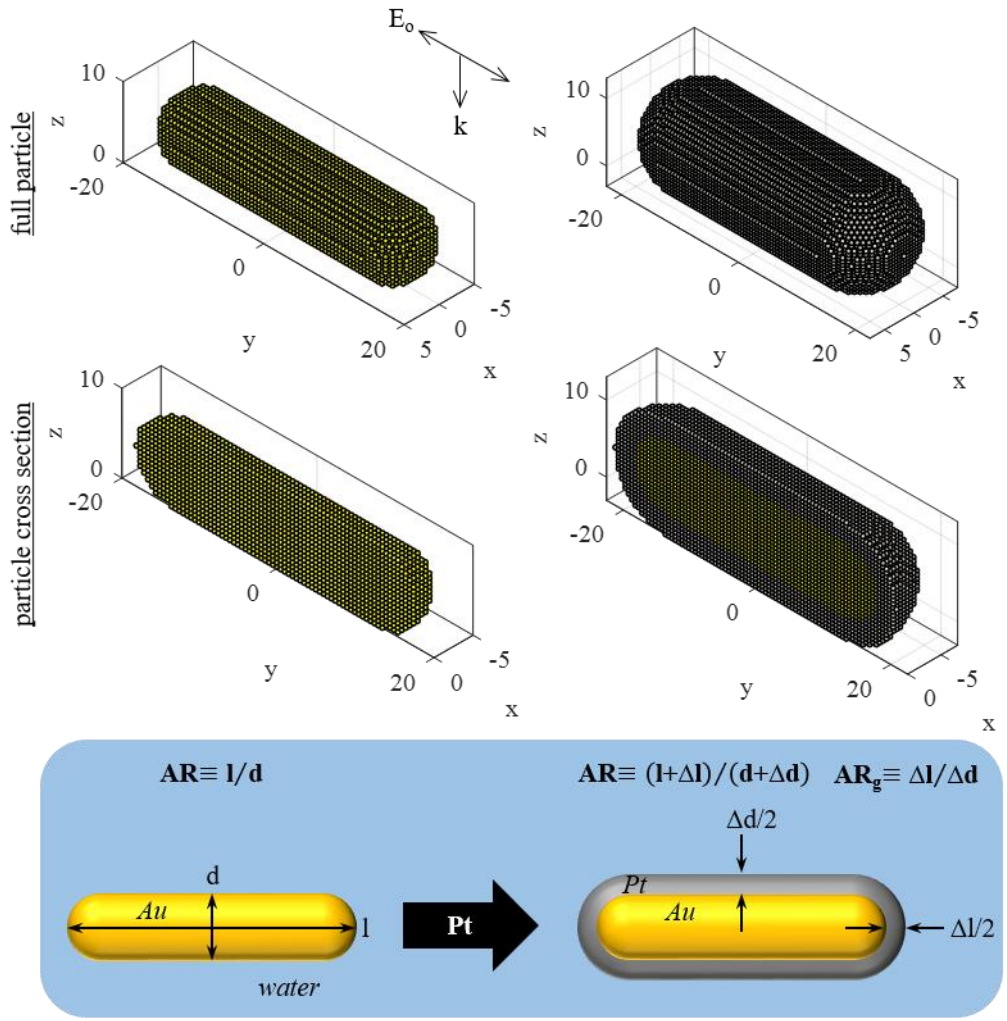

Figure S2. Schematic for DDA-representation of anisotropic core-shell growth of Pt (gray) onto AuNR (yellow). Top and middle panels show full-particle and x-z plane cross sections of point-dipole discretized DDA representations (i.e., targets), respectively. Bottom panel shows a cartoon cross section with defined spatial parameters, the overall aspect ratio (AR) and Pt shell growth aspect ratio (AR_g).

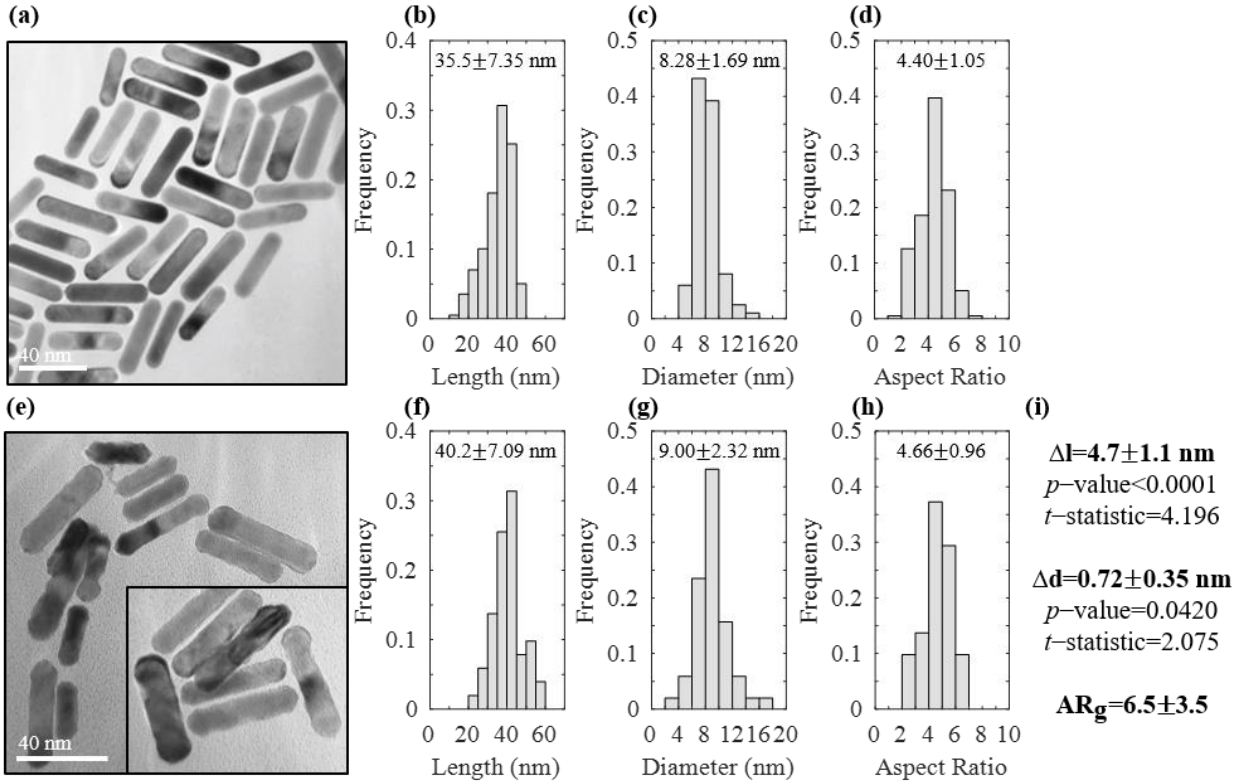

Figure S3. TEM statistical analysis of (top) AuNR and (bottom) AuNR after photoreduction of $PtCl_6^{2-}$. (a)/(e) are representative TEM images. Frequency histograms for total nanorod (b)/(f) length, (c)/(g) diameter, and (d)/(h) overall aspect ratio, AR, extracted from TEM are shown with inset mean±standard deviation of the Gaussian distributions. (i) Welch's t-test was performed to analyze changes to mean nanorod length and diameter (Δl and Δd, respectively) upon photodeposition of Pt, with uncertainty defined as the standard error of the difference. Mean length of the nanorod population increased from 35.5 nm to 40.2 nm with a two-tailed p value of <0.0001, which was statistically significant (99.99% confidence). Mean diameter of the nanorod population increased from 8.28 nm to 9.00 nm while standard deviation expanded from 1.69 nm to 2.32 nm, giving a two-tailed p value of 0.0420. This suggested with 95.8% confidence there was a non-0 change in nanorod diameter as a result of Pt photodeposition, but significance in its magnitude was ambiguous. Mean AR increased from 4.40 to 4.66 because of the 4.70 nm increase in overall length upon Pt deposition. The Pt growth AR, defined as Δl/Δd, was calculated to be 6.5±3.5. Sample size was N=199 for AuNR and N=51 for Pt-AuNR.

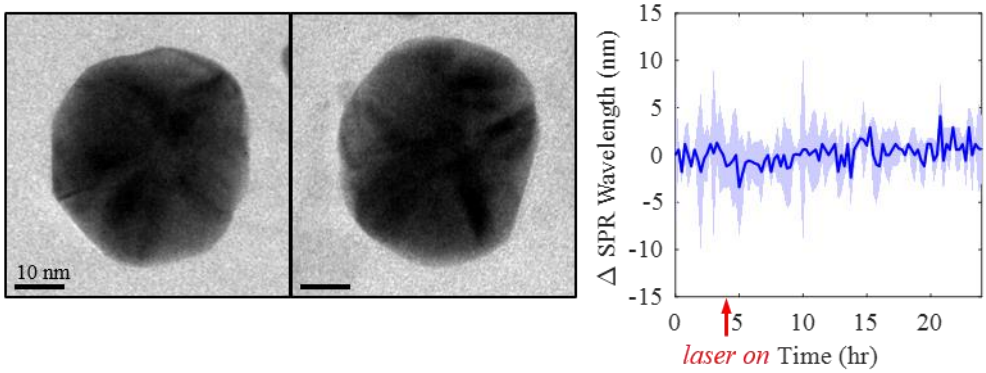

Figure S4. TEM images of washed Au nanospheres that were laser irradiated at 830 nm, off resonance of their SPR, in the presence of adsorbed $PtCl_6^{2-}$ (via $L_\pi MCT$ exceeding 273 nm) and methanol. Edges of the nanospheres in TEM appear identical before/after the reaction, suggesting Pt^0 did not occur. Transmission UV-vis monitoring of the SPR wavelength revealed no change during laser irradiation. A slight SPR blue shift was observed until hours ~3-4, thought to arise from a decrease in local refractive index after introducing methanol into the aqueous solution (see main manuscript). The SPR quickly returned to its initial wavelength (i.e., Δ SPR = 0) after equilibration where it held until the end of the experiment.

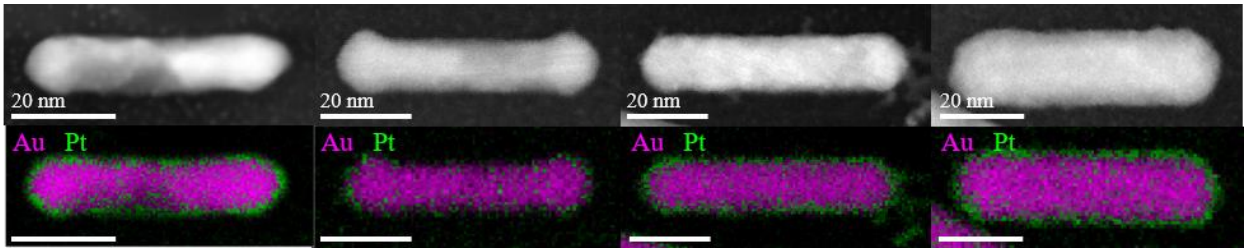

Figure S5. Representative EDS maps of Au and Pt from four Pt-AuNR processed using four uncorrelated variables with a principle component analysis (PCA). Each variable represented (i) Au (purple), (ii) Pt (green), (iii) carbon, and (iv) background (e.g., residual solvent, surfactant, etc.). Variables (iii) and (iv) were summed and colored black.

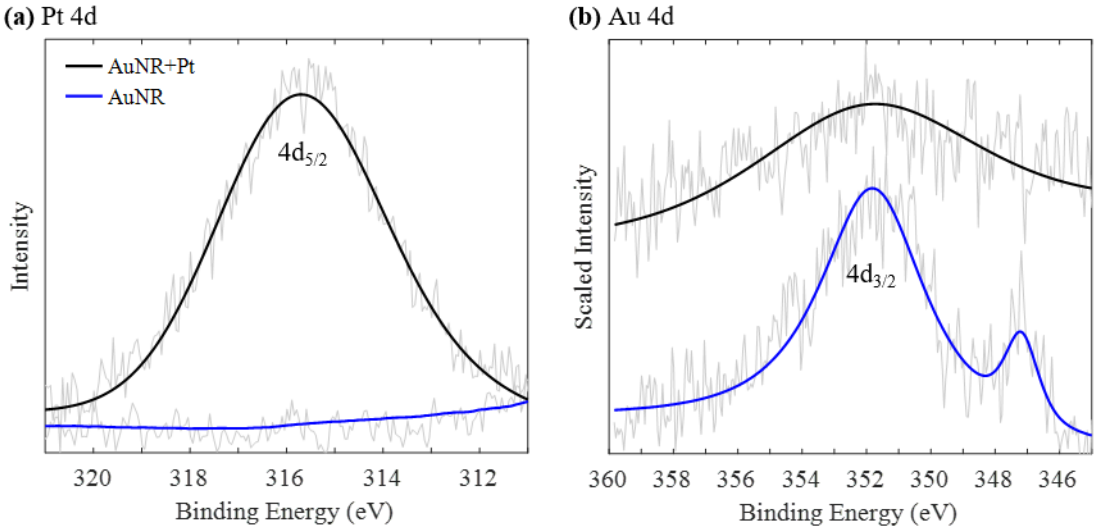

Figure S6. XPS spectra of (a) Pt 4d and (b) Au 4d lines of the AuNR irradiated at their LSPR in the presence of $PtCl_6^{2-}$, showing formation of Pt and a suppression of Au signal consistent with the Pt-Au shell-core morphology. Unlabeled feature in (b) at ca. 347 eV was ostensibly a satellite peak.

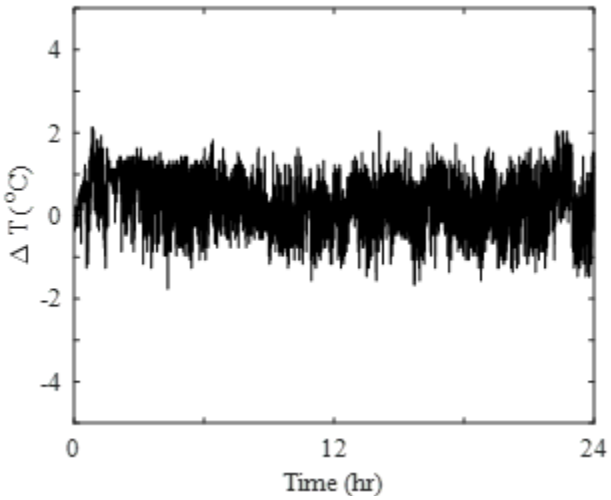

Figure S7. Change in cuvette surface temperature versus irradiation time measured by a thermocouple during 10 mW of 830 nm excitation of the AuNR to induce reduction of $PtCl_6^{2-}$. A mean ΔT of less than 0.3 ºC across the 24 hr timespan was measured. Total photodeposition trial was 36 hr, as shown in Figure 3, but the thermocouple ceased recording after 24 hr.

The plasmon-induced local change in temperature (ΔT_{NP}) by a non-spherical nanoparticle under continuous-wave, monochromatic irradiation may be expressed as:[1,2]

$$\Delta T_{NP} = \frac{I\sigma_{abs}}{4\pi r_{eff}\beta(AR)k_m} \quad \text{(S1)}$$

where I is the light intensity, σ_{abs} is the absorption cross section of the non-spherical particle with an effective radius, r_{eff}, calculated from an equi-volume sphere, β is a thermal-capacitance coefficient with dependence on the geometric aspect ratio (AR), and k_m is thermal conductivity of the surrounding media. I was measured to be (10 mW)/(π 1² mm²) = 3183 W m^{-2} ~ 3.2 W m^{-2}. DDA calculated σ_{abs} to be 1.12e-15 m² at 830 nm irradiation. The r_{eff} calculated from a sphere with total volume equal to the nanorods used in this work (taken as mean from TEM analysis) was 8 nm. The dimensionless β was calculated by 1+0.96587ln²(AR) = 1+0.96587ln²(4.40) = 3.12 according to work from Baffou *et al.*[2] The k_m was set to 0.6 W m^{-1} K^{-1} for water. The final calculated ΔT_{NP} using these values was 19 µK, which was negligible in the experiments.

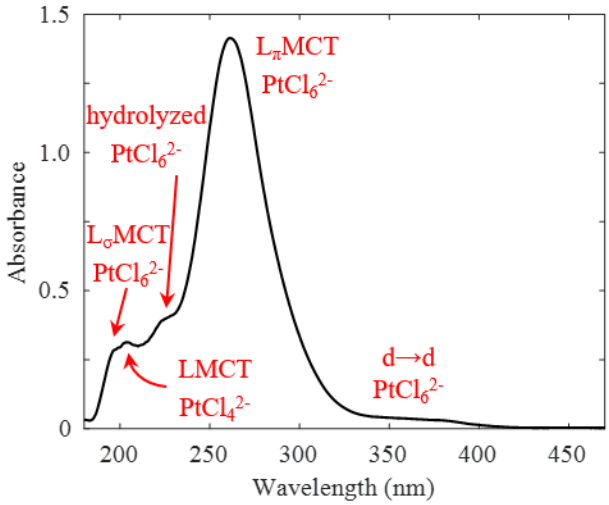

Figure S8. UV absorbance spectra of 83 µM H_2PtCl_6 in water. Ligand-metal charge transfer (LMCT) features and spin allowed d→d transition are labeled.

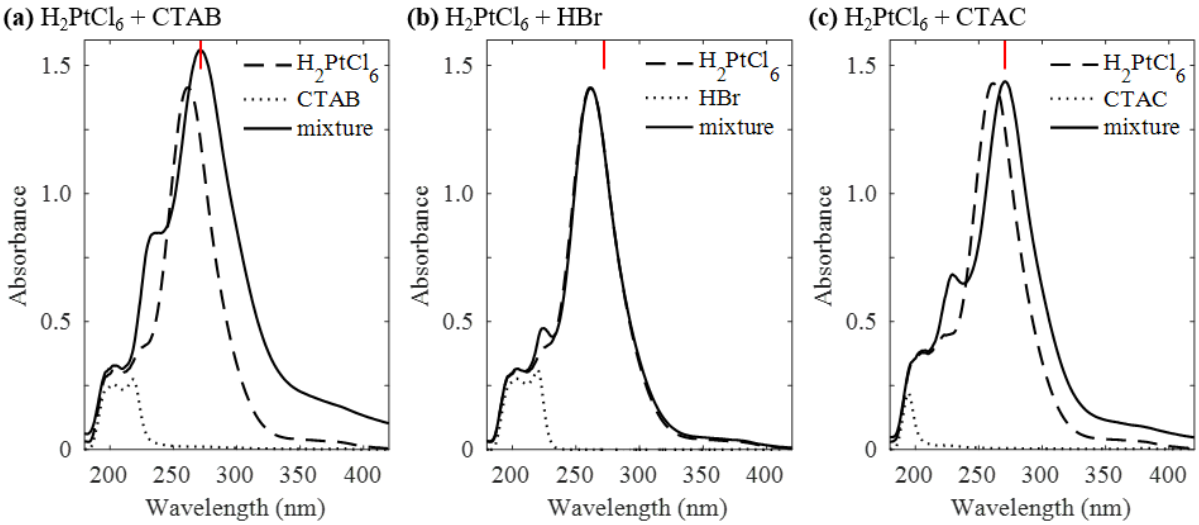

Figure S9. UV absorbance spectra of 83 µM H2PtCl6 mixed with 100x excess moles of (a) CTAB, (b) HBr, and (c) CTAC, a Cl- counter-ion analog for CTAB, in the dark. Negative control spectra for CTAB, HBr, and CTAC are shown (dotted). Red lines in each figure panel mark the 272 nm position for reference. LπMCT upon mixture with CTAB (i.e., CTA+ with Br- counter ions) occurred at 272 nm, marked with red lines for reference. LπMCT upon mixture with HBr (i.e., Br- ions) occurred at 261 nm. LπMCT upon mixture with CTAC (i.e., CTA+ with Cl- counter ions) occurred at 272 nm, matching results for CTAB complexation.

These spectra conclude (i) no Cl→Br ligand exchange of PtCl62- with dissociated Br- from the CTAB and (ii) LπMCT shift to 272 nm occurred from coordination with the trimethylammonium head groups of CTAB.

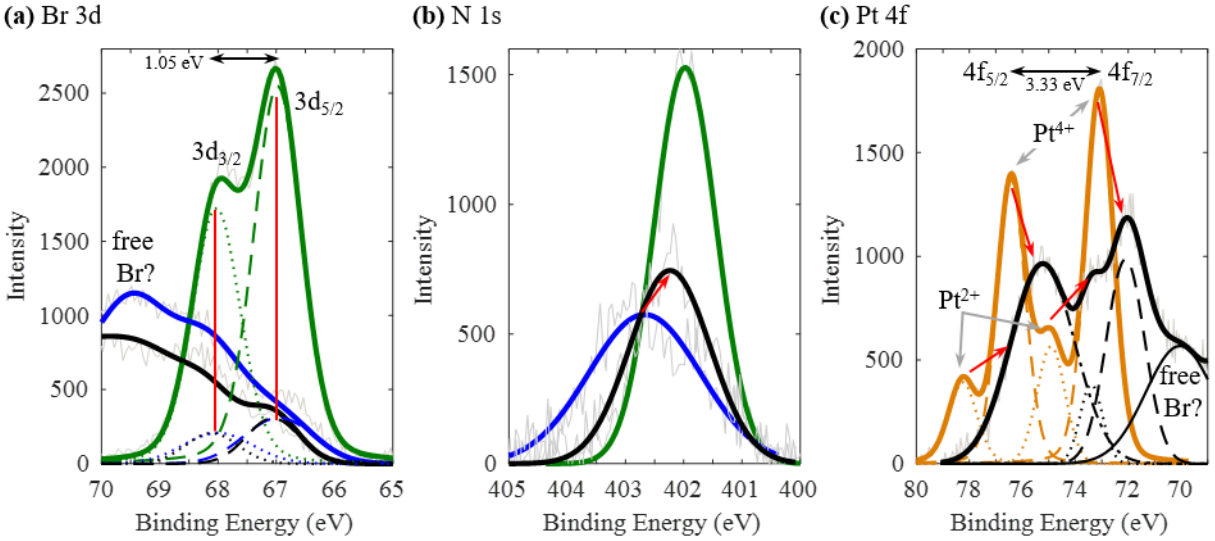

Figure S10. Shirley baseline-corrected XPS spectra of (a) Br 3d, (b) N 1s, and (c) Pt 4f lines measured from AuNR (covered in CTAB; blue), $PtCl_6^{2-}$ (orange), CTAB (green), and $PtCl_6^{2-}$ mixed with AuNR (black) in the dark. Red lines and arrows highlight important changes to the spectra. Dashed and dotted lines indicate fitted, correlated doublets underlying the composite spectra (solid). Binding energy for the Br 3d lines did not shift upon interaction with CTAB or AuNR and exhibited typical 1.05 eV spin-orbit separation. Binding energy for the N 1s peak shifted from 402.7 eV for AuNR down to 402.2 eV upon mixture with $PtCl_6^{2-}$; by comparison, pure CTAB exhibited a N 1s peak at 402.0 eV. Concomitantly, binding energies of the Pt^{4+} and Pt^{2+} 4f lines for $PtCl_6^{2-}$ decreased by 1.0 eV and 1.5 eV, respectively, upon complexation with the CTAB-covered AuNR. Both oxidized Pt species exhibited typical 3.33 eV spin-orbit separation between their respective 4f lines. The wide, dot-dashed fitted peak for $PtCl_6^{2-}$–AuNR mixture at 75.2 eV appeared to contain both the Pt^{4+} and Pt^{2+} $4f_{5/2}$ lines together. The line at 70 eV in (a) and (c) (*see blue and black spectra for AuNR and $PtCl_6^{2-}$–AuNR mixture, respectively) could be dissociated, free Br^- from the CTA; the Br $3d_{3/2}$ for CTAB [green in (a)], where Br^- was coordinated with the trimethylammonium CTA^+, appeared ca. 2 eV lower in binding energy that pure Br standards. Overall, these spectra agree with results from Figure S9 and conclude $PtCl_6^{2-}$ (i) did not undergo Cl→Br ligand exchange with dissociated Br^- from the CTAB and (ii) coordinated with the trimethylammonium N head groups of CTAB.

Quantity of CTAB present in the reaction mixture was estimated to be approximately 12:1 CTAB:Au and 60:1 CTAB:$PtCl_6^{2-}$, respectively, on a molarity basis. Ultimate CTAB concentration in the reaction mixture is fully dependent on execution of the AuNR stock solution washing step(s), where nearly 25% of the initial CTAB remains after each washing. The AuNR herein were synthesized in 93 mM CTAB and subjected to a 2x washing step to remove excess CTAB, which yielded approximately 6 mM final CTAB concentration (±50%) in the AuNR stock solution. Incomplete or excessive washing of the AuNR can result in more or less CTAB, respectively. In the 84:14 H2O:MeOH reaction mixture, this corresponded to 5 mM CTAB. The CTAB ligands on AuNR in this work concomitantly serve as (i) an agent to rapidly coordinate $PtCl_6^{2-}$ near the Au surface prior to diffusive adsorption onto the Au and (ii) polymer shell that impends/slows mass transport to the Au surface. Whether or not there exists an optimum CTAB concentration to promote plasmon-driven photoreduction onto colloidal nanoparticles is unclear, and likely depends on the metal nanoparticle surface area and number density. It is most desirable to have enough CTAB to form a bilayer on AuNR to maintain suspension while minimizing free CTAB so that $PtCl_6^{2-}$ is not "captured" away from AuNR. This would prevent interaction with AuNR. Although $PtCl_6^{2-}$-CTA^+ complexation was an important step towards allowing $PtCl_6^{2-}$ transport/adsorption to the AuNR for subsequent photodeposition in this work, this could merely be consequence unique to utilizing colloidal nanoparticle suspensions as hot electron sources. Surfactant-free nanoparticles, such as those obtained by metallization of a lithographed substrate, may readily offer clean surfaces for facile $PtCl_6^{2-}$ adsorption without the blockage by a polymer ligand that impends/slows mass transport.

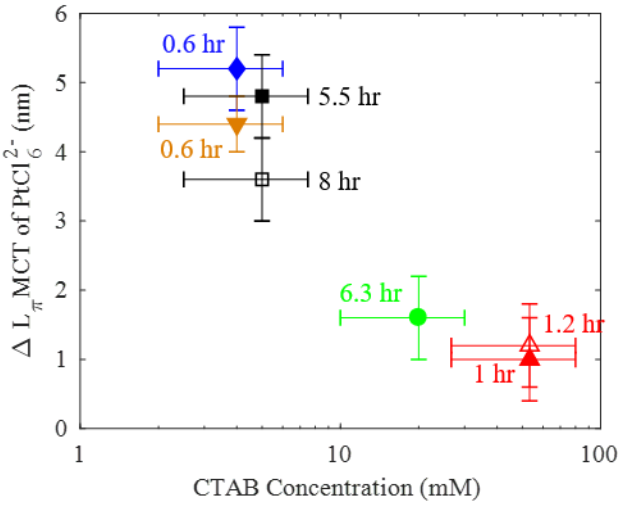

Figure S11. Change in L_πMCT wavelength of $PtCl_6^{2-}$ upon addition to CTAB-capped AuNR, indicative to the degree of adsorption to the Au surface, as a function of CTAB concentration in the reaction mixture. CTAB acts as a mass transport resistance. CTAB concentration of the $PtCl_6^{2-}$-AuNR growth solutions analyzed in the manuscript (black) were estimated to be ca. 5 mM by dependence on the preceding AuNR washing steps.=Labels are the measured time span for the L_πMCT to reach its given red-shift value. Colors indicate different AuNR batches and filled (open) indicate light (dark) trials. Here, Δ L_πMCT = 0 is 272 nm (i.e., $PtCl_6^{2-}$ coordinating with CTA^+) and Δ L_πMCT = 6 is 278 nm (i.e., $PtCl_6^{2-}$ adsorbing to Au surface).

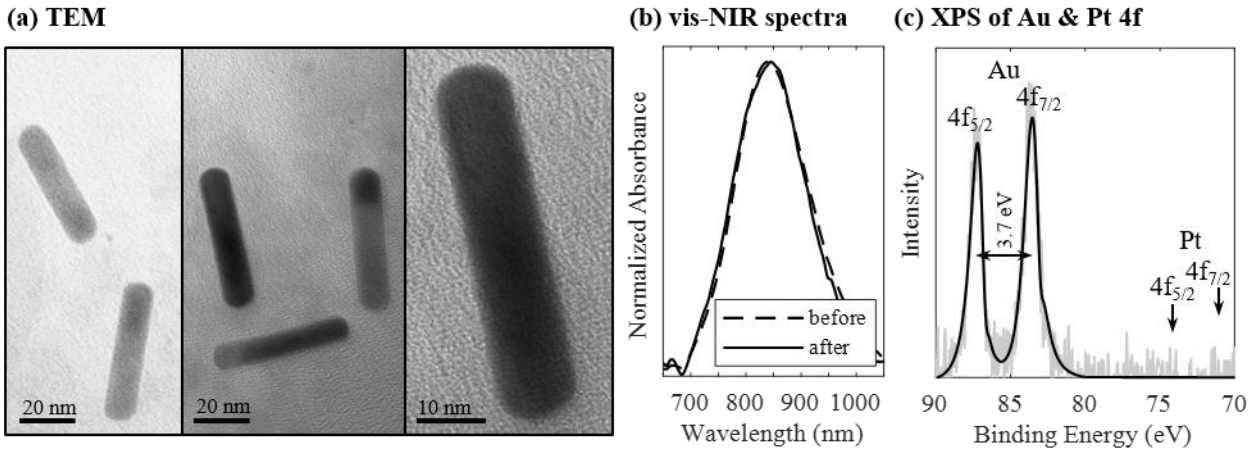

Figure S12. (a) TEM images of washed AuNR that were laser irradiated at 830 nm in presence of $PtCl_6^{2-}$, but the L_πMCT did not red-shift beyond 272 nm. In other words, the AuNR were excited at their LSPR without $PtCl_6^{2-}$ adsorbed to their surface and thus precluded photoreduction to Pt^0 by plasmonic hot electrons. Surface of the irradiated nanorods after washing appeared pristine and smooth, unlike those for Pt-AuNR in Figure 1(b). (b) The LSPR of the nanorods measured by transmission UV-vis spectroscopy before and after 830 nm laser irradiation appeared unchanged. (c) Shirley baseline-corrected XPS analysis of the nanorods after 830 nm excitation and washing at the Au and Pt 4f photoelectron lines, showing no detectable Pt.

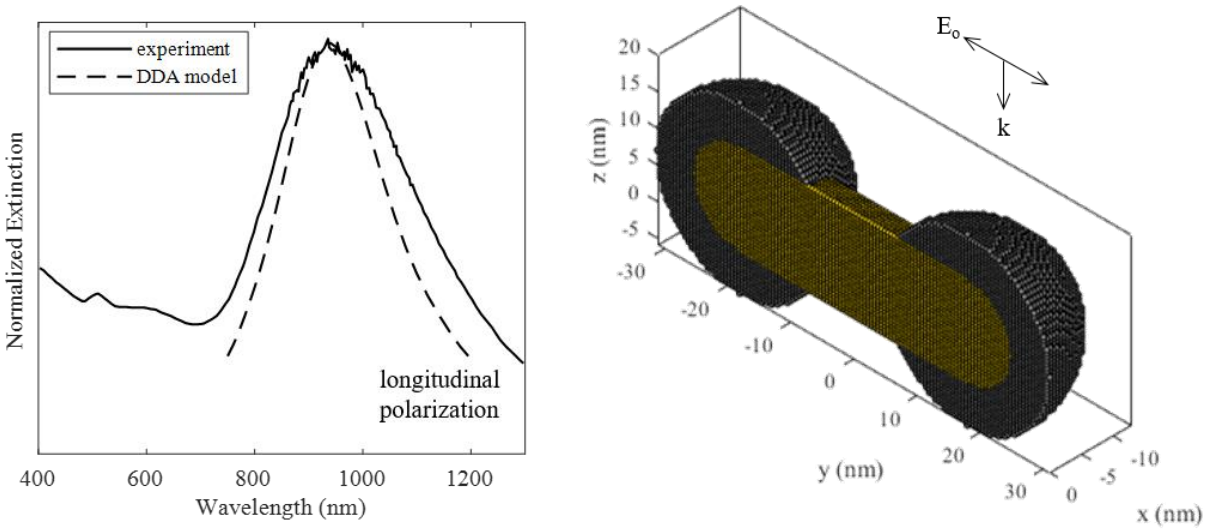

Figure S13. DDA-calculated optical extinction spectra from longitudinal-polarization of a Pt-decorated AuNR with dumbbell morphology compared with measured absorbance spectra in a cuvette by Zheng *et al*.[3] Size parameters in the DDA were chosen verbatim according to the reported TEM statistics. A cross-section of the DDA target is shown.

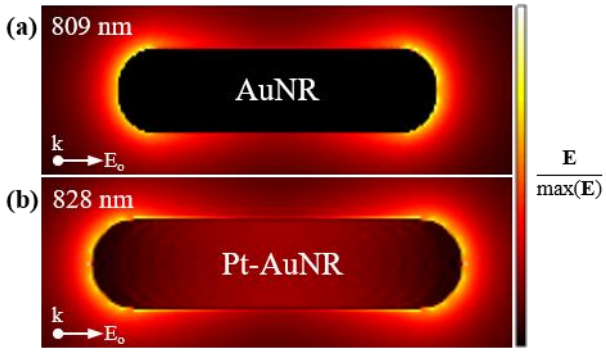

Figure S14. Enhanced electric near-field plots calculated by the DDA for (a) AuNR and (b) Pt-AuNR. AuNR dimensions were 9×36 nm, giving a LSPR at 809 nm. Pt-AuNR dimensions were 9.5×40.5 nm, giving a LSPR at 828 nm. Dimensions in the DDA were based on those extracted experimentally from TEM, which showed the rod length and width grew from 35.5 nm to 40.2 nm and from 8.3 nm to 9.0 nm, respectively.

Plane-wave density functional theory (DFT) calculations were carried out using the CASTEP code.[4] Geometry optimizations were performed with the BFGS minimization algorithm for Au, Pt-Au and Pt supercells.[5-6] The Perdew-Becke-Ernzerhof (PBE) functional in the generalized gradient approximation (GGA) was adopted with a relativistic (Koelling-Harmon) and spin-unrestricted formalism.[7] For slab supercell calculations, ultrasoft Pt and Au pseudopotentials were employed. The supercell calculations were evaluated with precise level FFT grid parameters to yield a good representation of the electron density with a plane-wave basis energy cut-off of 400 eV. The electronic minimization was evaluated with a Pulay density mixing scheme and setting a fine SCF convergence threshold for the total energy to less than 1×10^{-6} eV atom^{-1}. Slab supercell simulations were performed for (100) and (111) orientations for Pt, Au that were cleaved along [100] and [111] directions and built into a Pt-Au supercell with a thickness of 7 layers and a 20 Å vacuum. Additional slab supercells with 9 layers and a 20 Å vacuum were performed for comparison, whereby it was determined that the 7-layer thickness was sufficient to describe the valence band spectra of the Pt-coated AuNR. For all slab calculations, the top 2 layers were allowed to relax, whereas the remaining layers were constrained to the initial fractional coordinates determined by separate primitive cell calculations. For all periodic slab calculations, a self-consistent dipole correction was utilized. The Monkhorst-Pack scheme for all calculations was utilized with a k-point separation of 0.02 Å^{-1} for Brillouin Zone sampling with the eigenvalues obtained from the calculation smeared by 0.2 eV (black lines in Figure S15).[8] The total density of states (TDOS) and partial projected density of states (PDOS) were obtained for all optimized slab supercells and compared for each layer within the simulation.

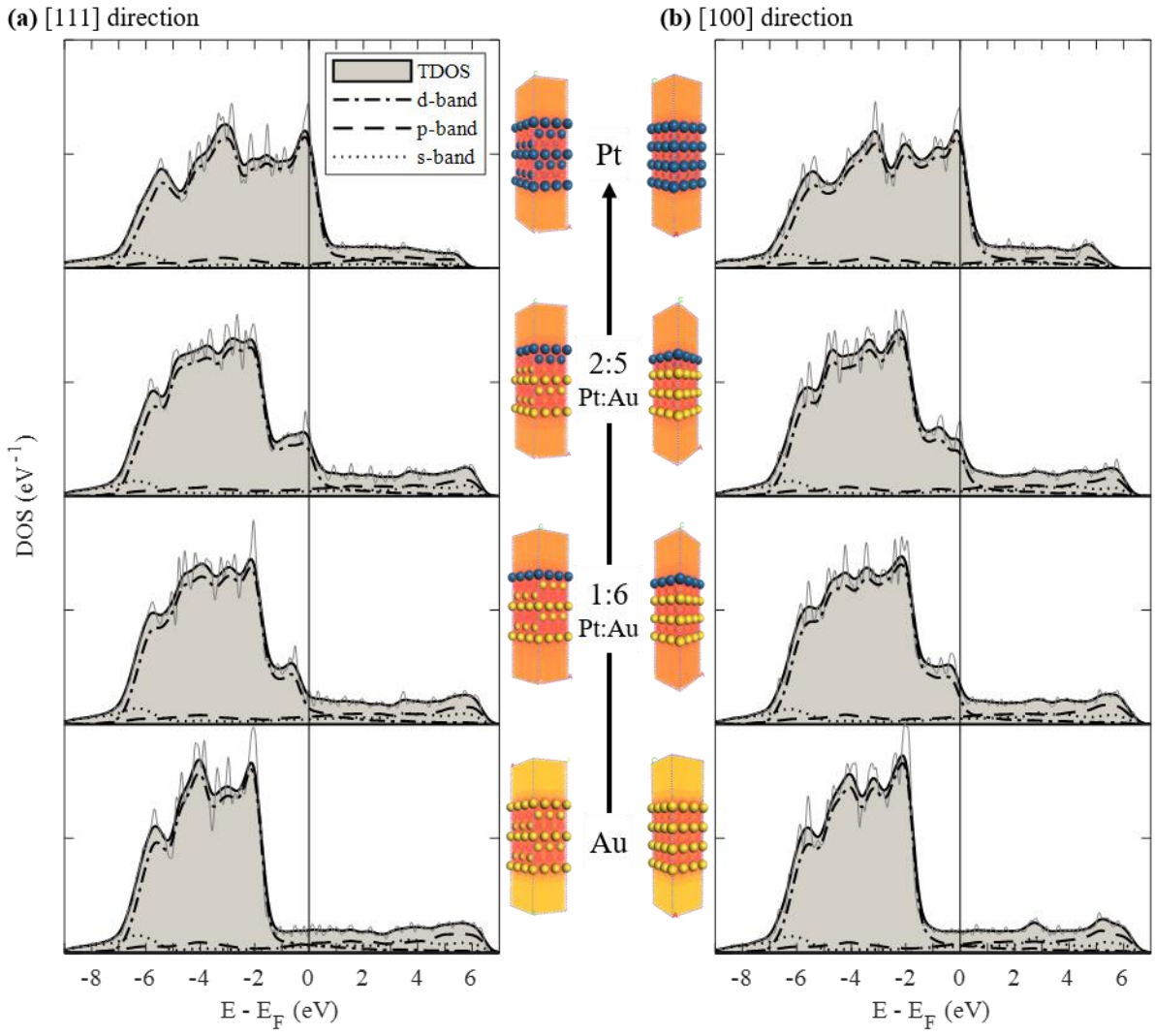

Figure S15. Total DOS (TDOS; gray shaded with black solid line) summed from partial DOS contributions from the *s*-, *p*-, and *d*-band orbitals calculated by DFT for "bulk" Au upon monolayer deposition of Pt (at 1:6 and 2:5 Pt:Au ratios) that eventually converge to "bulk" Pt. (a) shows the planes along [111] and (b) shows the planes along [100]. Simulation target representations are shown in the center, where Au are yellow spheres and Pt are dark blue spheres. Energy scale is relative to the Fermi level, E_F, where positive values approach vacuum (i.e., smaller absolute energy). A 0.2 eV smearing was applied to smooth the raw calculated DOS, which is analogous to DOS measured by XPS where the detector has a finite instrument function that limits energy resolution.

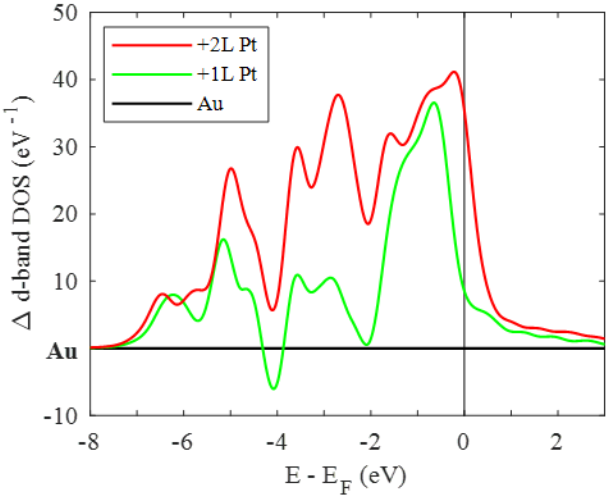

Figure S16. Change in *d*-band DOS along [111] relative to "bulk" Au upon addition of 1- and 2-monolayers layers of Pt, showing progressive increase in *d*-band states near the Fermi level, E_F. Here, Δ d-band DOS = 0 is defined as pure Au. Energy scale is relative to the Fermi level, E_F, where positive values approach vacuum (i.e., smaller absolute energy).

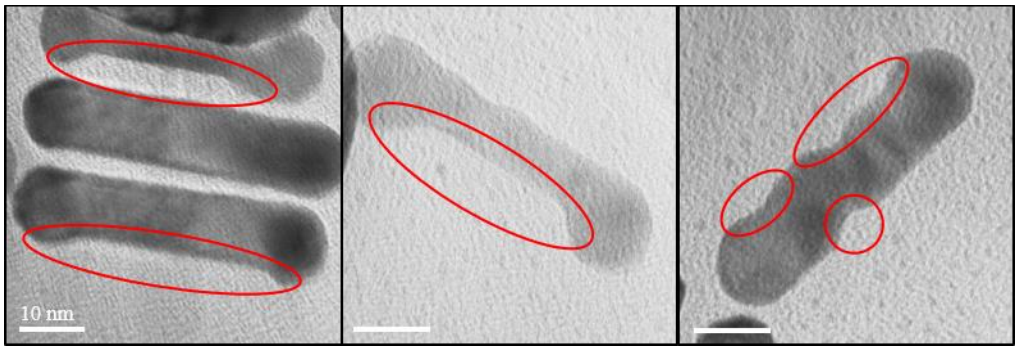

Figure S17. TEM micrographs of apparent oxidation sites of AuNR after resonant laser-induced photoreduction of $PtCl_6^{2-}$ to Pt^0 in the absence of a sacrificial hole scavenger to complete the oxidation half reaction, leaving behind oxidized Au. These sites, circled in red, ostensibly represented the sites of plasmonic hot holes as shown in Figure 5. MeOH was used as a hole scavenger in this work.

REFERENCES

(1) Guo Guo, J.; Zhang, Y.; Shi, L.; Zhu, Y.; Mideksa, M. F.; Hou, K.; Zhao, W.; Wang, D.; Zhao, M.; Zhang, X.; et al. Boosting Hot Electrons in Hetero-Superstructures for Plasmon-Enhanced Catalysis. *J. Am. Chem. Soc.* **2017**, 139 (49), 17964–17972.

(2) Baffou, G.; Quidant, R.; García de Abajo, F. J. Nanoscale Control of Optical Heating in Complex Plasmonic Systems. *ACS Nano* **2010**, 4 (2), 709–716

(3) Zheng, Z.; Tachikawa, T.; Majima, T. Single-Particle Study of Pt-Modified Au Nanorods for Plasmon-Enhanced Hydrogen Generation in Visible to Near-Infrared Region. *J. Am. Chem. Soc.* 2014, 136 (19), 6870–6873.

(4) Clark Stewart, J.; Segall Matthew, D.; Pickard Chris, J.; Hasnip Phil, J.; Probert Matt, I. J.; Refson, K.; Payne Mike, C., First principles methods using CASTEP. In *Zeitschrift für Kristallographie – Cryst. Mater.* **2005**, *220*, 567.

(5) Payne, M. C.; Teter, M. P.; Allan, D. C.; Arias, T. A.; Joannopoulos, J. D., Iterative minimization techniques for ab initio total-energy calculations: molecular dynamics and conjugate gradients. *Rev. Mod. Phys.* **1992**, *64* (4), 1045-1097.

(6) Pfrommer, B. G.; Côté, M.; Louie, S. G.; Cohen, M. L., Relaxation of Crystals with the Quasi-Newton Method. *J. Comp. Phys.* **1997**, *131* (1), 233-240.

(7) Perdew, J. P.; Burke, K.; Ernzerhof, M., Generalized Gradient Approximation Made Simple. *Phys. Rev. Lett.* **1996**, *77* (18), 3865-3868.

(8) Monkhorst, H. J.; Pack, J. D., Special points for Brillouin-zone integrations. *Phys. Rev. B* **1976**, *13* (12), 5188-5192.